AIAA AVIATION Forum
August 2-6, 2021, VIRTUAL EVENT
AIAA AVIATION 2021 FORUM

10.2514/6.2021-2559

Lift Enhancement for Supersonic Delta Wing at Low Speed Using CoFlow Jet

Zhijin Lei *Gecheng Zha †
Dept. of Mechanical and Aerospace Engineering
University of Miami, Coral Gables, Florida 33124
E-mail: gzha@miami.edu

Abstract

Numerical study is carried out to investigate flapped delta wing low speed performance with coflow jet (CFJ) flow control at Mach number of 0.1. Two delta wings formed by thin supersonic airfoils with aspect ratio of 2 and 0.67 and sweep angle of 53° and 63.5° are studied, but only the detailed results for the wing with aspect ratio of 2 are presented. The simulation is validated very well with the experiment. The flap has a constant chord along span and is 24% of the root chord. CFJ is applied in two ways: one on top of the main front part of the delta wing and the other is on the deflected flap. Both are effective, but the CFJ applied on the deflected flap is much more effective with flow attached up to the flap deflection angle of 60°. It has substantially higher lift coefficient enhancement and lower CFJ power consumption for the same C_μ.

With $C_\mu = 0.08$ and CFJ applied on the flap, the delta wing with AR of 2 improves C_L by 113.1% at a flap deflection angle of 60°, whereas $(C_L/C_D)_c$ is about the same as that of the baseline delta wing with no flow control at the same flap deflection angle.

Trade studies are conducted to investigate the effect of delta wing incidence angle (β), flap deflection angle (δ), CFJ injection slot location, CFJ momentum coefficient C_μ. The trade study of the incidence angle shows that the CFJ used on the flap is effective at least up to β of 20° with the appearance of the delta wing leading edge vortex. The flap deflection angle study indicates that the baseline delta wing's lift coefficient becomes flat when the flap deflection angle is greater than 30°, whereas the delta wing with CFJ flap has the lift coefficient increased linearly to the deflection angle of 60° studied. The trade study of the injection location shows that the lift and drag coefficient are decreased about 5% when the injection is moved from upstream of the flap deflection shoulder to downstream of the shoulder, but the CFJ power coefficient is reduced by 50%. The injection momentum coefficient trade study indicates that the lift coefficient is enhanced most rapidly at low C_μ value range from 0.01 to 0.04 with a steep slope, whereas the CFJ power coefficient P_c increases at a slower pace. At C_μ of 0.03, the CFJ flapped delta wing achieves C_L of 1.23, C_L/C_D of 4.21, and $(C_L/C_D)_c$ of 4.034. Compared with the baseline flapped delta wing with C_L of 0.856 and C_L/C_D of 3.64, the CFJ delta wing achieves an increase of lift coefficient by 44% and C_L/C_D by 15.6% respectively with the CFJ power coefficient of 0.013.

This study is only an initial effort to apply CFJ flow control to thin supersonic delta wing with a flap. It shows that CFJ is very effective to substantially increase lift coefficient at very low energy expenditure, which has great potential to enhance the supersonic aircraft's low-speed performance.

Nomenclature

CFJ	Co-flow Jet
SST	Supersonic (Civil) Transports

* Ph.D. Candidate
† Professor, ASME Fellow, AIAA associate Fellow

SST	Suction Surface Translation
AR	Aspect Ratio
AoA	Angle of Attack
LE	Leading Edge
TE	Trailing Edge
MAC	Mean Aerodynamic Chord Length
Ma	Mach Number
PR	Pressure Ratio
U	Flow Velocity
U_{inj}	Flow Velocity in Injection Slot
U_∞	Freestream Flow Velocity
P	Pumping Power
C_L	Lift Coefficient $L/(q_\infty S)$
C_D	Drag Coefficient $D/(q_\infty S)$
C_μ	Jet Momentum Coefficient $\dot{m}_j U_j/(q_\infty S)$
$(C_L/C_D)_c$	CFJ Airfoil Corrected Efficient $L/(q_\infty S V_\infty)$
S_{wing}	Wing Area
$S_{Takeoff}$	Takeoff Distance
$\dot{m}$	Mass Flow
c	Chord Length
q	Dynamic Pressure $0.5\,\rho U^2$
p_t	Mass-averaged Static Pressure
β	Angle of Incidence
δ	Flap deflection Angle
h	Slot Size (width)
x/c	Slot Location (Streamwise)
l_{duct}	Slot Length (Spanwise)
θ	Injection Slot Location (defined by hinge)
γ	Specific Heat Ratio
η	Pump Efficiency
ρ	Air Density
∞	Free Stream Conditions
$_j$	Jet Conditions
$_{inj}$	Injection slot
$_{suc}$	Suction slot

1 Introduction

Supersonic Civil Transports (SST) is an important sector in aviation industry. High efficiency and low sonic boom are crucial for the SST's economic viability. The higher the cruise speed, the more difficult to meet the stringent requirements of low speed, which determines the community noise and runway length. One challenge for supersonic aircraft at low speed is to achieve a high lift coefficient, which is difficult to obtain when the wing is highly swept and formed with thin airfoil with low aspect ratio.

As shown in Table 1, Concorde needs a runway of about 12,000 ft to take off, which almost exceeds the longest runway of the New York JFK Airport. NASA's SST N+2 Program expects that 30-passenger supersonic business jets and 100-passenger commercial jets limit their takeoff runway requirements to be less than 9,000 fts[1].

Table 1: C_{Lmax}, S_{wing}, $S_{Takeoff}$ and Takeoff Velocity of Existing SSTs, compared with B767-200ER.

Aircraft	Weight, lb	C_{Lmax}	S_{wing}, ft^2	$S_{Takeoff}$, ft	Takeoff Velocity, mph
Tu-144LL[2, 3]	455,950	0.612	5,450	9,613	220
Concorde[4]	400,000	0.77	3,856	11,800	250
B767-200ER[5]	395,000	$\simeq 2$	3,050	8,150	140-190(B767-300)

Table 1 shows the maximum takeoff lift coefficient, wing area and required takeoff runway length of Concorde, Tu-144LL and B767-200ER(as comparison). It can be seen that, if the maximum lift coefficient of the two SST during takeoff can be increased to the level of transonic transports, the run way length can be reduced to below 9,000 ft.

Mavris *et al*[6] employ Circulation Control (CC) to enhance HSCT low speed lift coefficient[7]. For some configurations, the CC can reduce the takeoff field length by 31%, the liftoff speed by 11%, and the obstacle height speed by 10%. However, CC needs to use engine bleed, which may not be always available, in particular at landing when the engines are mostly idle.

The purpose of this paper is to enhance the lift coefficient of 3D highly swept Delta wings at low speeds by using coflow jet active flow control with minimized energy expenditure. The study is important to lay a foundation for high performance supersonic civil transport design.

1.1 Co-Flow Jet (CFJ) Active Flow Control

The CFJ recently developed by Zha *et al*[8, 9, 10, 11, 12, 13, 14, 15, 16, 17, 18, 19] is demonstrated to achieve large lift augmentation, stall margin increase, drag reduction and moderate nose-down moment for stationary and pitching airfoils. In a CFJ airfoil, an injection slot near the leading edge (LE) and a suction slot near the trailing edge (TE) on the airfoil suction surface are created. As shown in Fig. 1, a small amount of mass flow is drawn into the suction duct, pressurized and energized by the micro compressor, and then injected near the LE tangentially to the main flow via an injection duct. The whole process does not add any mass flow to the system and hence is a zero-net-mass-flux(ZNMF) flow control.

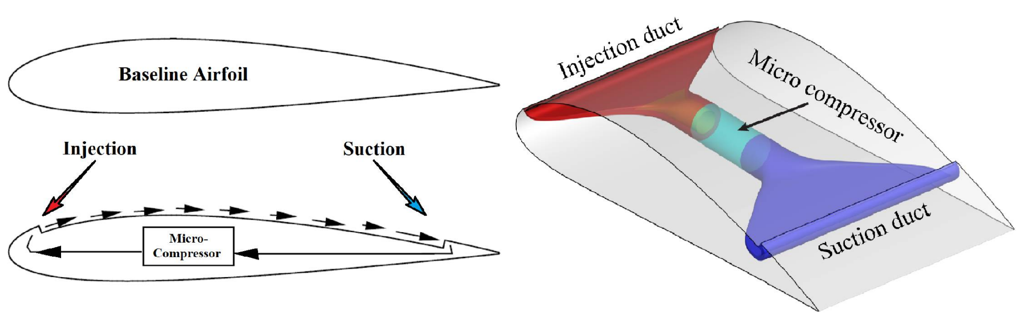

Figure 1: Schematic plot of a typical CFJ airfoil.

For CFJ airfoil, we usually have the suction surface (upper surface) slightly translated downward to accommodate the tangential injection jet. It is named suction surface translation (SST).

The research so far on CFJ airfoil and wing mainly focuses on thick ones. This study is the first effort to apply CFJ to 3D highly swept Delta wings formed by thin supersonic airfoil at low speeds to enhance the lift coefficient with minimized CFJ power consumption.

1.1.1 CFJ Parameters

The following are some important parameters used for CFJ active flow control. The jet momentum coefficient C_μ is a parameter used to quantify the jet intensity and is defined as:

$$C_\mu = \frac{\dot{m}U_j}{\frac{1}{2}\rho_\infty {U_\infty}^2 S} \tag{1}$$

where $\dot{m}$ is the injection mass flow, V_j is the mass-averaged injection velocity, ρ_∞ and V_∞ denote the free stream density and velocity, and S is the planform area.

The power consumption is determined by the jet mass flow and total enthalpy change as the following:

$$P = \dot{m}(H_{t1} - H_{t2}) \tag{2}$$

where H_{t1} and H_{t2} are the mass-averaged total enthalpy in the injection cavity and suction cavity respectively, P is the Power required by the pump and $\dot{m}$ the jet mass flow rate.

The total power can be expressed with the pump efficiency η and total pressure ratio of the pump $\Gamma = \frac{P_{t1}}{P_{t2}}$ as:

$$P = \frac{\dot{m}C_p T_{t2}}{\eta}(\Gamma^{\frac{\gamma-1}{\gamma}} - 1) \tag{3}$$

where γ is the specific heat ratio equal to 1.4 for air. Eq. 3 indicates that the CFJ power is determined exponentially by the total pressure ratio and linearly by the mass flow rate. This provides a guideline to minimize the energy expenditure by using larger injection slot size to have lower total pressure loss and higher mass flow[20, 21, 22, 23, 24, 25].

$$P_c = \frac{P}{\frac{1}{2}\rho_\infty V_\infty^3 S} \tag{4}$$

For a CFJ wing, a corrected aerodynamic efficiency that includes the CFJ power coefficient is defined as:

$$(\frac{C_L}{C_D})_c = \frac{C_L}{C_D + P_c} \tag{5}$$

Eq. 5 is mainly for the purpose to compare the aerodynamic efficiency with conventional aircraft with no active flow control that has $P_c = 0$. A more comprehensive parameter termed productivity efficiency measuring the aircraft transportation productivity represented by $R \times W$ (Range $\times$ Gross weight) is defined as[21]:

$$(\frac{C_L^2}{C_D})_c = \frac{C_L^2}{C_D + P_c} \tag{6}$$

2 Numerical Approaches

2.1 CFD Code

An in-house CFD code FASIP (Flow-Acoustics-Structure Interaction Package) is used to conduct all the numerical simulations. The 2-D Reynolds-Averaged Navier-Stokes (RANS) equation is solved with one-equation Spalart-Allmaras turbulence model. A 5th order WENO scheme for the inviscid flux and a 2nd order central differencing for the viscous terms are employed to discretize the Navier-Stokes equations. The low diffusion E-CUSP scheme used as the approximate Riemann solver suggested by Zha *et al*[26] based on the Zha-Bilgen flux vector splitting scheme [27] is utilized with the WENO scheme to evaluate the inviscid fluxes. Implicit time marching method using Gauss-Seidel line relaxation is adopted to achieve a fast convergence rate [28]. Parallel computing is implemented to save wall-clock simulation time. The RANS solver is validated for CFJ static airfoil simulation[29, 12, 13, 14, 15, 16, 17, 18, 19, 20, 21, 22, 23, 24, 25]. The wall treatment suggested in [30] to achieve the 3rd order accuracy is employed.

To achieve zero-net mass-flux with the CFJ flow control, the injection mass flow must be equal to the mass flow entering the suction slot. Additionally, the jet strength must be controlled in order to reach the prescribed C_μ. This is achieved by iterating the jet total pressure until the C_μ value is within 1% of the prescribed value. At the suction, the suction mass flow is matched to the injection mass flow by iterating the static pressure at the suction cavity. The process is iterated throughout the simulation until the specified momentum coefficient is achieved and the injection and suction mass flow match.

2.2 Baseline Models, Meshes and Validation

The baseline wings, shown in Fig. 2 (left), are formed by flat supersonic airfoil designed by McKinney Jr *et al*[31]. Only half of the wings are simulated due to symmetry of the geometries as illustrated on the right of Fig. 2. The baseline airfoil thickness is constant in the front part and is linearly decreased in the rear part. The rear part with the thickness decreasing is treated as a flap to implement CFJ by assuming a hinge is added in the center. The CFJ injection is implemented at the location with the thickness starting to decrease.

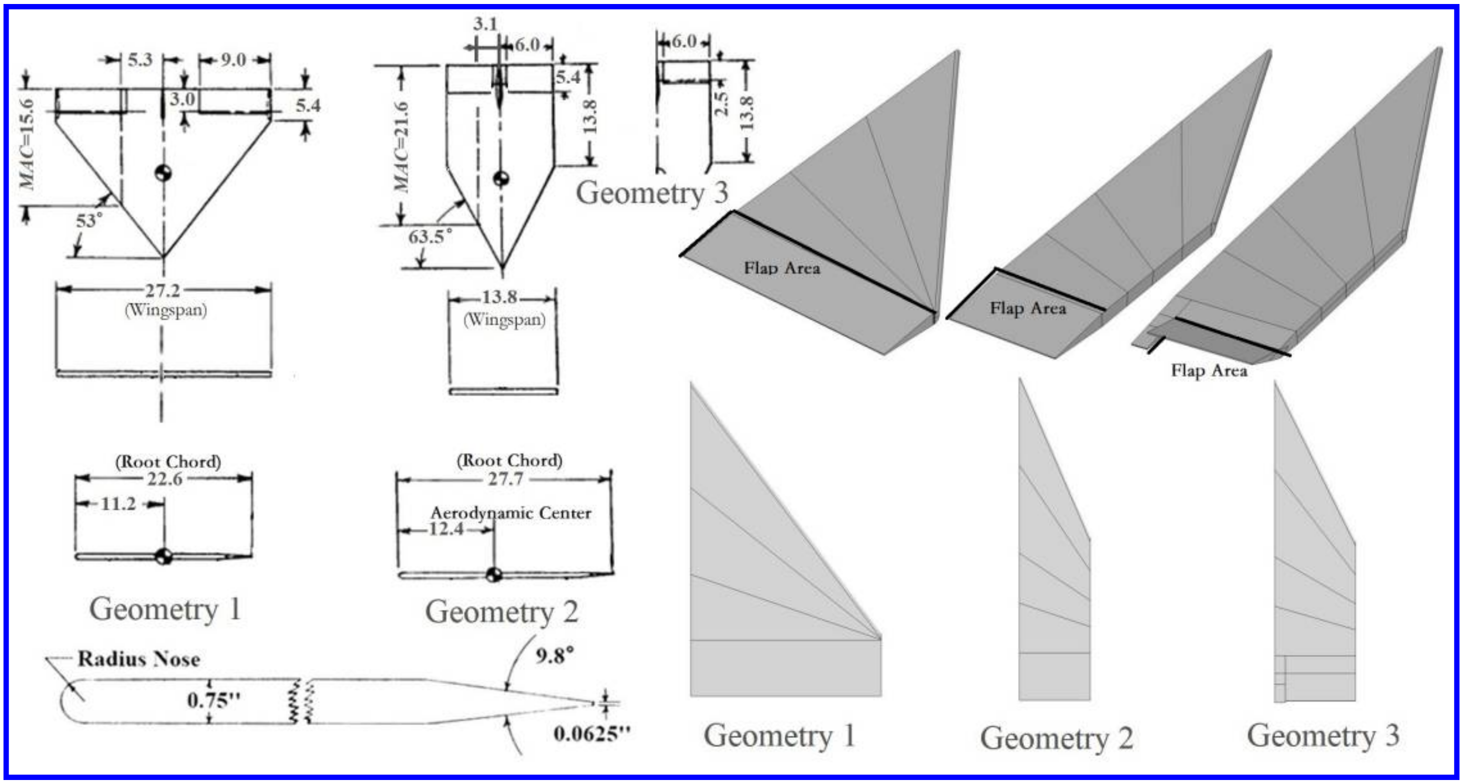

Figure 2: Airfoil section and baseline wing geometries for validation, from [31].

In Fig. 2, the Geometry 1 is adopted from the free-flight Model-2 in [31] with the vertical tail and landing gear removed. The Geometry 2 is adopted from the Model-5 in [31] with the same treatment. Their geometry characteristics are given in Table. 2.

Table 2: Aerodynamic characteristics of the wing geometries.

Name	AR	LE Swept Angle	MAC/c_{root}	Wingspan/c_{root}	Thickness	c_{flap}/c_{root}
Geometry 1	2.0	53°	0.673	1.203	4.8%	24%
Geometry 2	0.67	63.5°	0.780	0.498	2.7%	20%
Geometry 3	0.67	63.5°	0.780	0.498	2.7%	10%

The thickness is defined based on the mean aerodynamic chord length(MAC). The Geometry 3 in Fig. 2 is the same as the Geometry 2, but has a flap turned up 20°. It is used only to validate the 3D baseline simulation.

The computation mesh is constructed using the O-mesh topology in order to achieve high quality around the airfoil. Split into 61 blocks, the total baseline mesh has a size of 810k nodes, where 300 points are used to describe the airfoil section. To resolve the turbulent boundary layer, the thickness of the first layer around the surface has $y_+ = 1$. Three refined meshes are generated with the mesh size shown in Table 3 for mesh dependence analysis. The finest one is refined with 500% more cells and $y_+ = 0.5$. It can be seen that, at $AoA = 5°$ and the given flow conditions, the CFD result is mesh indepenednt when the mesh size is no smaller than 1.47M nodes.

Table 3: Aerodynamic coefficients comparison of Geometry 1 at $AoA = 5°$, Re=4.1531×10^5.

Data	Ma	C_L yielded
Experiment[31]	0.015	0.1579
CFD, Mesh Size of 810k Nodes ($300 \times 45 \times 60, Coarse$)	0.015	0.1613
CFD, Mesh Size of 1.47M Nodes ($410 \times 60 \times 60, Medium$)	0.015	0.1576
CFD, Mesh Size of 2.95M Nodes ($410 \times 120 \times 60, Fine$)	0.015	0.1549
CFD, Mesh Size of 1.47M Nodes ($300 \times 70 \times 70$)	0.015	0.1553

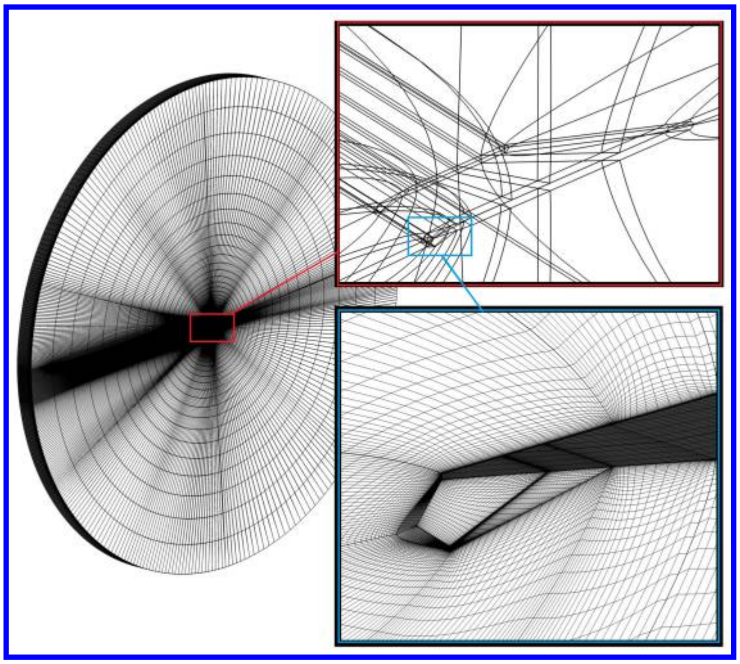

Figure 3: A mesh of the Baseline Geometry 3.

A mesh topology for Geometry 3 is shown in Fig. 3. The radius of farfield calculation zone is 100 times of the MAC of the wing. The distance from symmetric plane to spanwise far field boundary is 10 times' length of the wingspan. The comparisons of the lift and drag coefficient between the experiment and the CFD prediction with mesh refinement, are shown in Fig. 4 and Fig. 5. The CFD results of geometries matches experiment data well.

The medium mesh size achieves the mesh independent solutions and is used for all the studies in this paper. For CFJ meshes, the regions around CFJ injection and suction are refined.

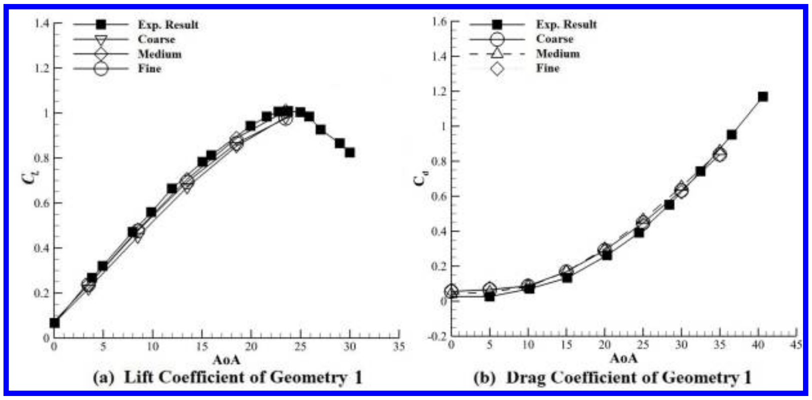

Figure 4: Mesh-independence validation, C_L(a) and C_D(b) of Geometry 1.

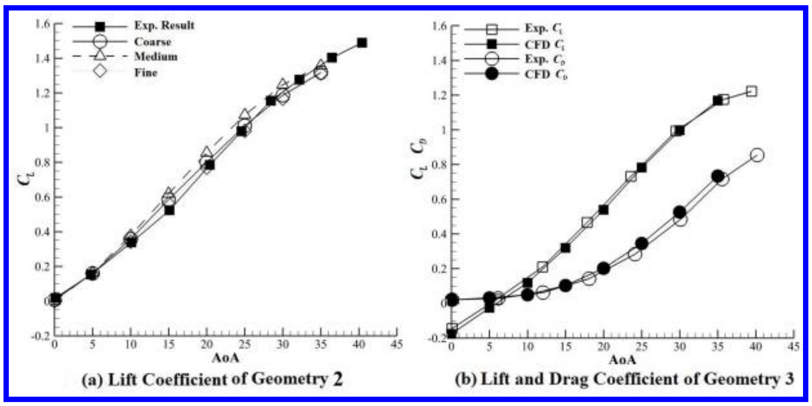

Figure 5: Mesh-independence validation, C_L(a) of Geometry 2, and C_L, C_D comparison of experimental data and medium mesh of Geometry 3(c).

2.3 CFJ Design

Two CFJ configurations are designed based on Geometry 1 and Geometry 2.

Table 4: Aerodynamic coefficients comparison of Geometry 1 at $AoA = 5°$.

Name	SST/MAC	h_{inj}/MAC	h_{suc}/MAC	$(x/c)_{inj}$	$(x/c)_{suc}$	l_{duct}/Wingspan
CFJ-1-Geometry-1	0.001	0.015	0.045	LE	flap hinge	0.85
CFJ-2-Geometry-1	0.003	0.015	0.075	flap hinge	0.25MAC to TE	1
CFJ-1-Geometry-2	0.001	0.015	0.045	LE	flap hinge	1
CFJ-2-Geometry-2	0.003	0.015	0.075	flap hinge	0.25MAC to TE	1

Fig. 6 shows the flapped baseline and CFJ wing geometries. The comparison is made between CFJ wings and the new flapped Baseline Geometries, as shown in Fig. 6(a). CFJ wings are named after prefix "CFJ-1" or "CFJ-2". Table 4 describes the name and basic geometric features of them. The CFJ-1 is to have the CFJ implemented on the main part of the wing as shown in Fig. 6(b). The CFJ-2 is to have the CFJ implemented on the flap as shown in Fig. 6c). Total pressure, total temperature and flow angle are specified as the inlet boundary conditions for the upstream side of the far-field boundary and inside the injection cavity. Constant static pressure is used downstream at the far-field boundary and in the suction cavity.

The suction slot width of all geometries are fixed as the best performing configuration of Liu *et al*[32].

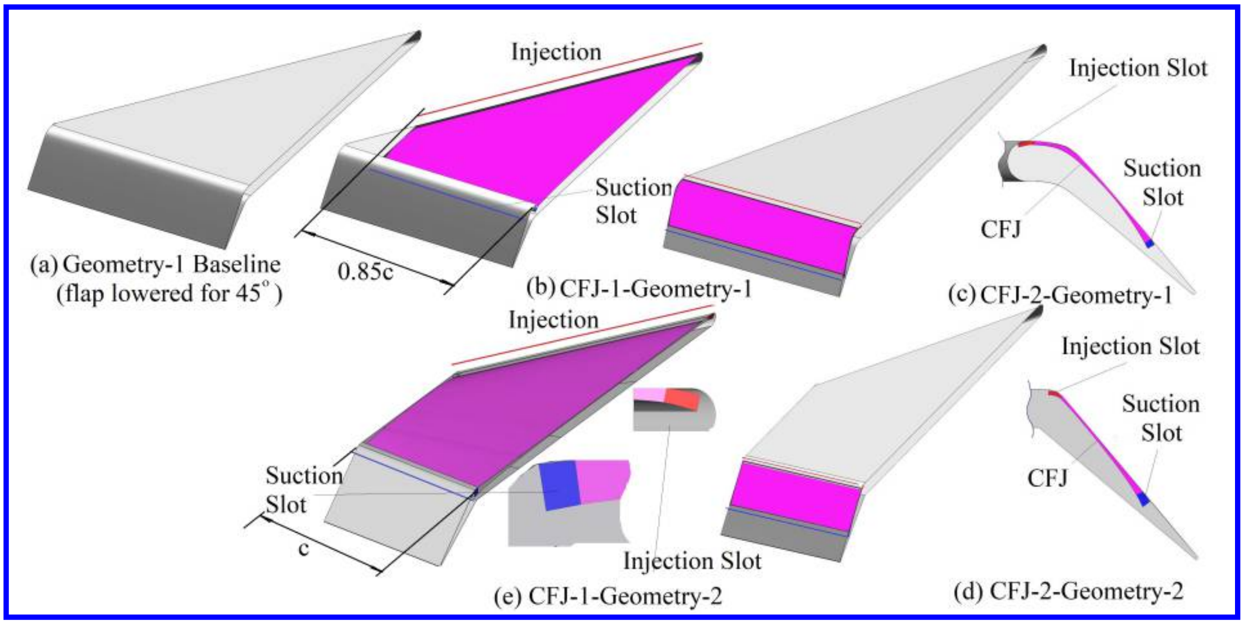

Figure 6: (a) CFJ-Geometry-1-Baseline; (b) CFJ-1-Geometry-1; (c) CFJ-2-Geometry-1; (d) CFJ-2-Geometry-2 and (e)CFJ-2-Geometry-1.

3 Results and Discussion

The simulation is performed with the freestream condition of Ma=0.1 and $Re = 4.1531\times10^5$.

3.1 Flow-field and power characteristics of the CFJ-implemented airfoils

A flapped Geometry-1, CFJ-1-Geometry-1 and CFJ-2-Geometry-1 are simulated to investigate the flow field with varied incidence and CFJ implementation. Both CFJ wings have a fixed C_μ of 0.08, the angle of incidence β of 0°, and flap deflection angle δ of 45°. β can be considered as the angle of attack of the constant thickness front part of the delta wing. The Mach contours of the flow fields are shown in Fig. 7.

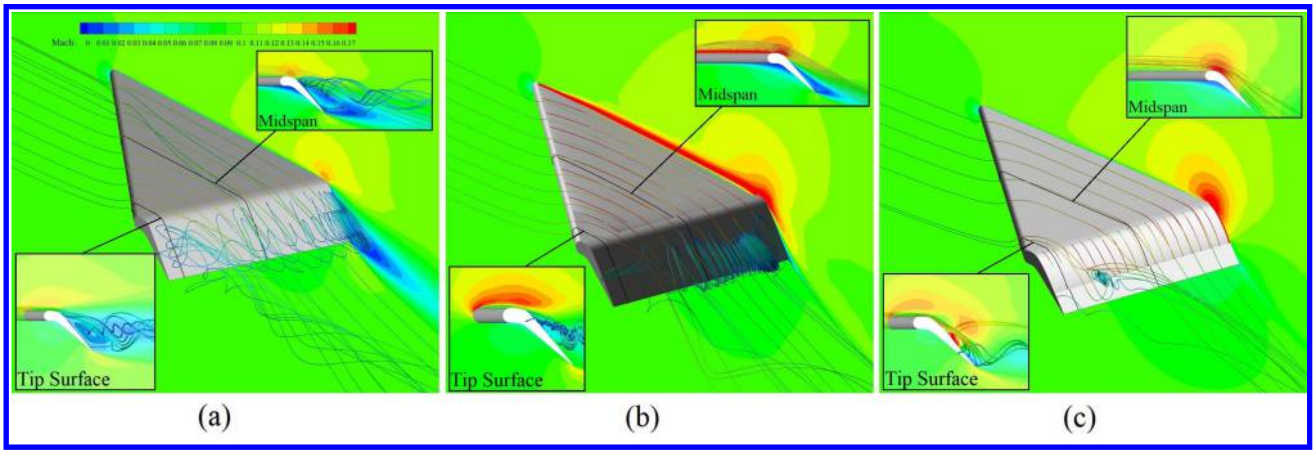

Figure 7: Mach contour of Geometry-1 baseline(a), CFJ-1(b) and CFJ-2(c), δ = 45°, β = 0°, θ=65°, CFJ C_μ=0.08.

Fig. 7(a) shows the flow is attached on the upper surface of the baseline flapped wing, but is massively separated in the flap region. When the CFJ is implemented on the suction surface of CFJ-1 geometry(b), the flow on the upper surface is more energized and accelerated and the separation on the flap is reduced, especially in the near-root region, but mild separation still exist. However, when a CFJ is implemented on the flap of CFJ-2 geometry(c), the separation on the flap is removed except there is a tip vortical flow as shown in Fig. 7(c).

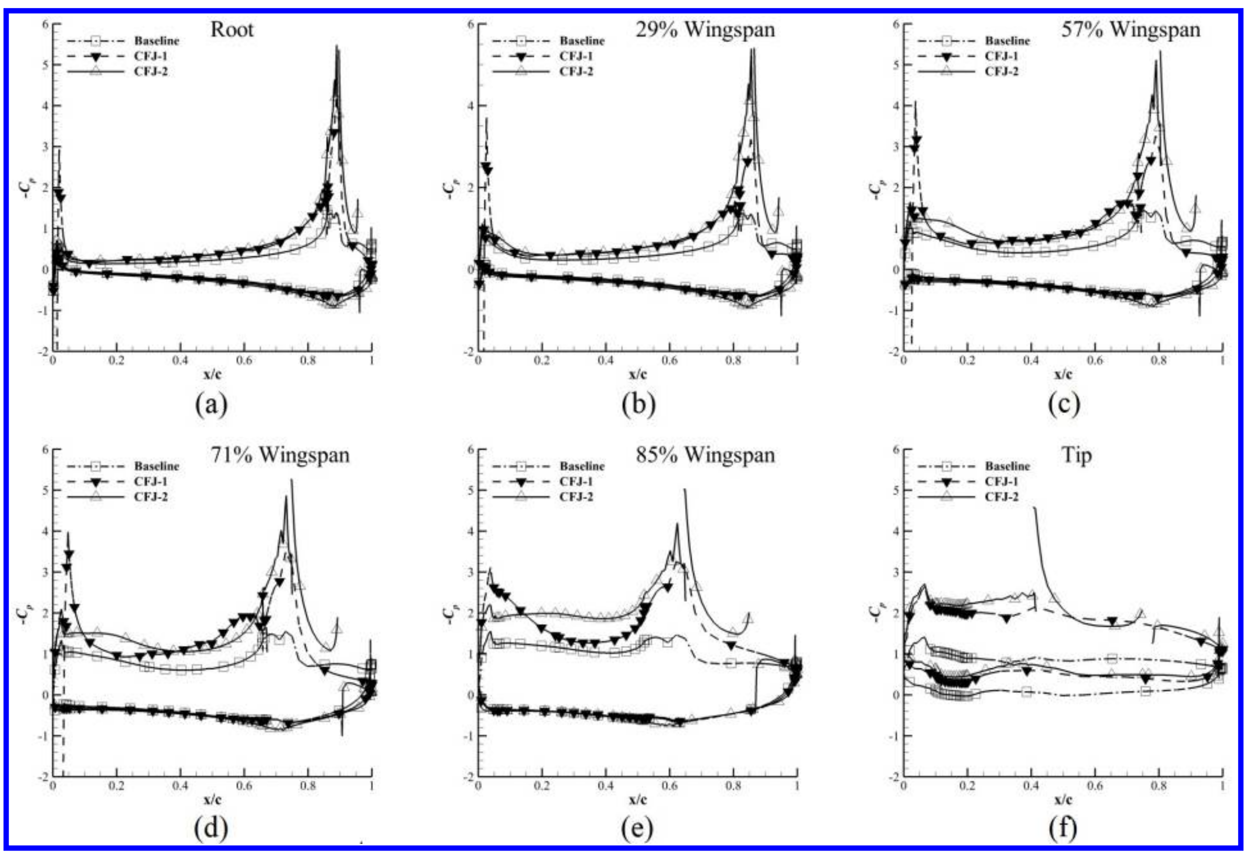

Figure 8: Pressure distributions of the Baseline Geometry-1, CFJ-1-Geometry-1 and CFJ-2-Geometry-1 around the wing sections at root(a), 29%(b), 57%(c), 71%(d), 85%(e) of wingspan, and tip region(f).

Fig. 8 shows the pressure distributions of the Baseline Geometry-1, CFJ-1-Geometry-1 and CFJ-2-Geometry-1 around the wing sections along spanwise direction. The largest pressure difference of both geometries occurs near the flap deflection location which has the largest turning of the wing profile. It can be observed that, in the near-root region, the CFJ-1-Geometry-1 and CFJ-2-Geometry-1 has a similar effect of enlarging the pressure difference between pressure surface and suction surface, while in the near-tip region CFJ-2 works slightly more effective.

Table 5: C_L, P_c and $(C_L/C_D)_c$ of Model-2 Geometries, β=0°, δ=45°, CFJ C_μ=0.08.

Geometry	C_L	C_D	P_c	C_L/C_D	$(C_L/C_D)_c$	$\delta C_L/P_c$	δC_L	U_{inj}/U_∞	PR
Baseline	0.8564	0.2351	0	3.6427	3.6427	0	0%	-	-
CFJ-1	1.0992	0.2283	0.1592	4.8147	2.8366	1.5251	28.4%	1.649	1.047
CFJ-2	1.3122	0.3165	0.0349	4.1460	3.7342	13.0602	53.2%	2.79	1.017

Table 5 shows C_L, P_c, $(C_L/C_D)_c$ and CFJ-introduced C_L increase of different geometries at β=0°. It is clear that, under the same C_μ=0.08, CFJ-2 simultaneously enhance C_L and reduce energy consumption. It enhances C_L by 53.2% and the $(C_L/C_D)_c$ is even slightly increased compared with baseline.

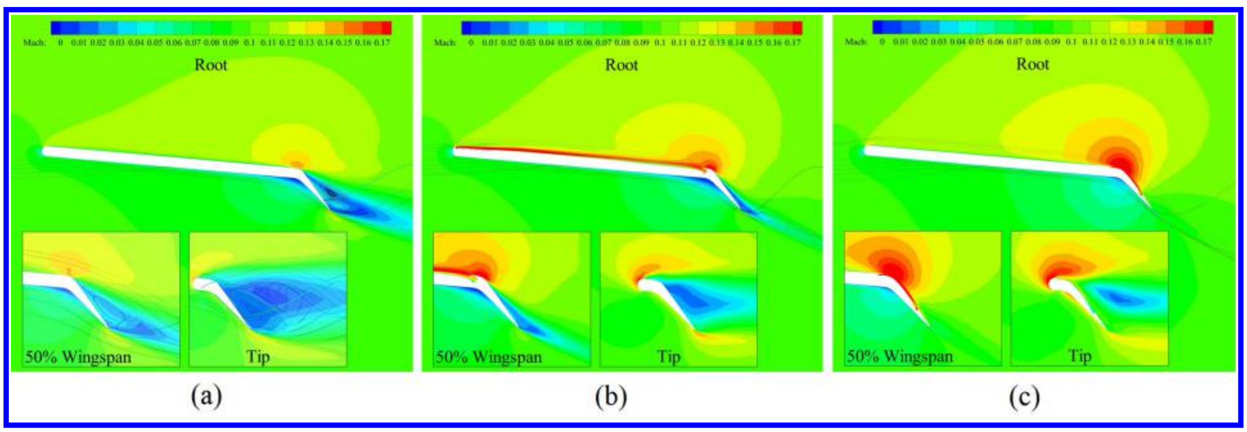

Figure 9: Mach number contours of Geometry-1 baseline(a), CFJ-1(b) and CFJ-2(c), δ = 45°, β = 5°, θ=65°, CFJ C_μ=0.08.

Fig. 9 are the Mach contours of Geometry-1 at incidence angle β of 5°. The overall angle of attack is also increased. The baseline Geometry-1 still has a massive separation on the flap. Both the CFJ-1 and CFJ-2 geometry 1 have the flow well attached on the flap.

Fig. 10 shows the Mach contours with streamlines at β at 10°, 16°, and 20°. At β of 10°, there is a weak leading edge vortex formed. With the β increasing, the LE vortex becomes stronger. The lift coefficient of CFJ-2-Geometry-1 start to decrease when β is greater than 11°, but the lift coefficient is still substantially higher than the baseline at the same β. The CFJ makes the flow still attached on the flap beneath the LE vortex emanating from upstream. For the baseline geometry, the lift is slightly increased when β is greater than 10°, but substantially lower than the CFJ-Geometry.

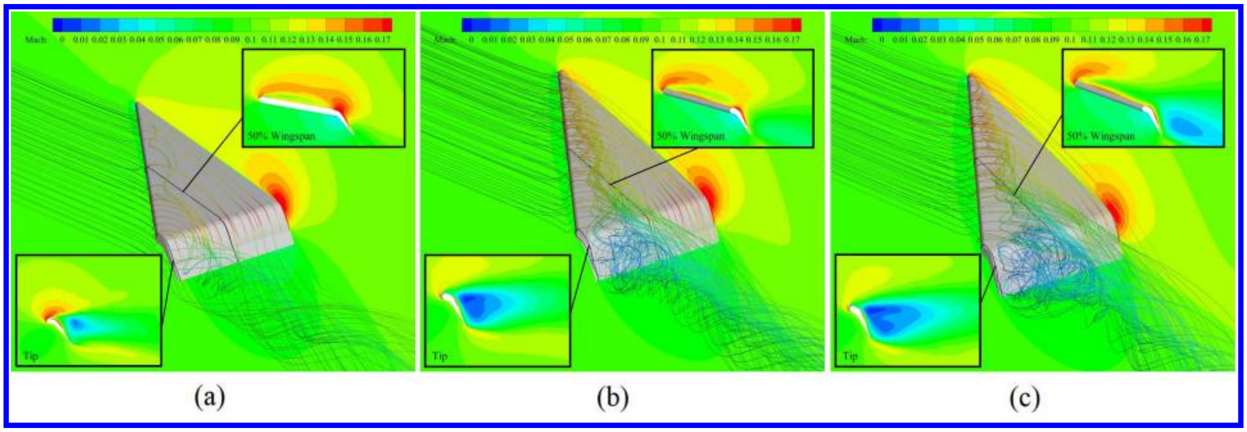

Figure 10: Evolution of the flow over suction surface when β is increased from 10°(a) to 16°(b) and 20°(c).

The aerodynamic coefficient of lift, drag, and CFJ power etc of CFJ-2-Geometry-1 versus its angle of incidence β is shown in Fig. 11.

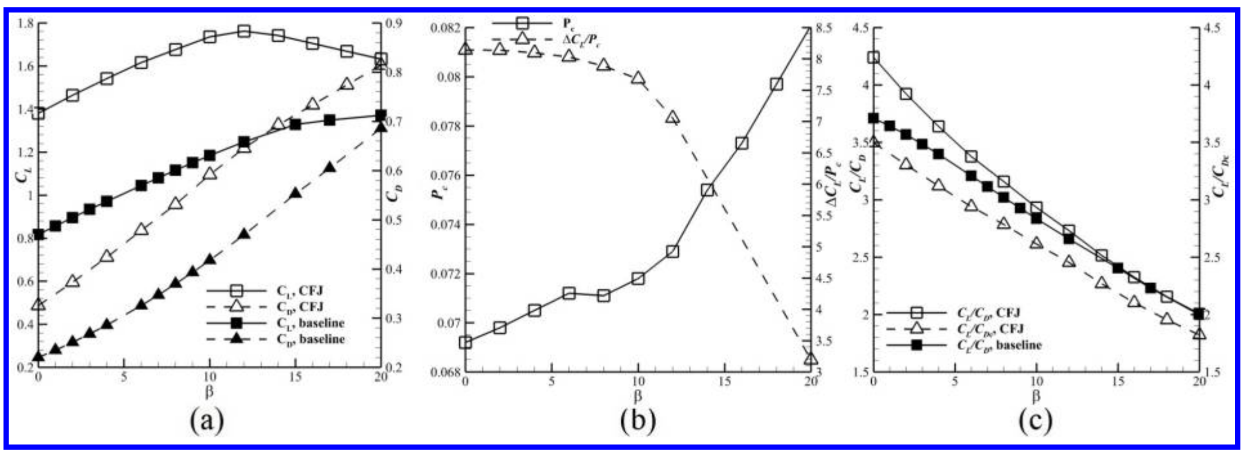

Figure 11: C_L, C_D, P_c, (C_L/C_D), $(C_L/C_D)_c$ and $\Delta C_L/P_c$ of CFJ-2-Geometry-1 versus β. C_μ=0.08, δ=45°.

To study the sweep and aspect ratio effect, the CFJ is applied to Geometry 2, which has an aspect ratio of 0.67 and sweep angle of 63.5°. As compared in Table 2, the Geometry 2 is much more 3-dimensional than Geometry 1. Fig. 12 shows the Mach contour of its baseline(a), CFJ-1(b) and CFJ-2(c) geometries, The CFJ works as effectively as for Geometry 1 to attach the flow, in particular when it is applied on the flap.

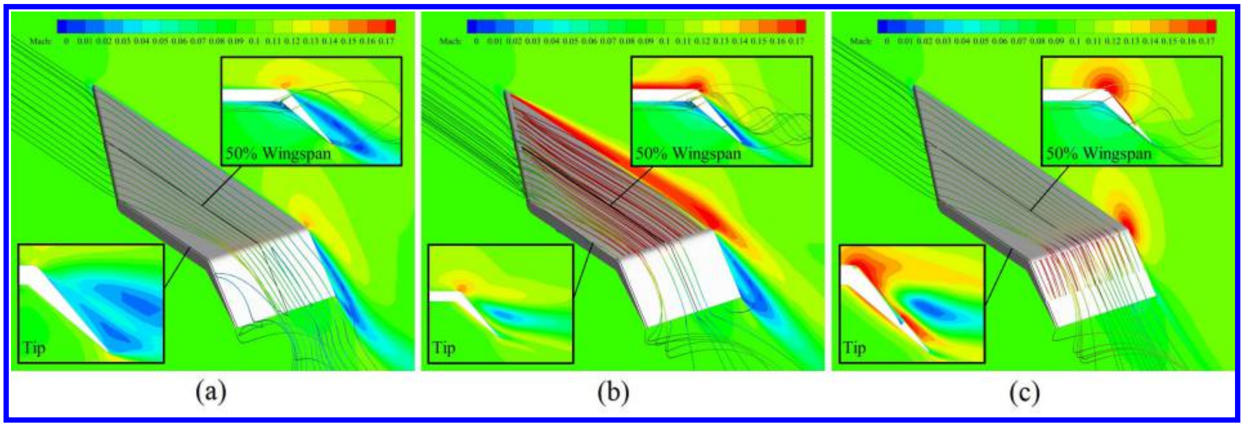

Figure 12: Mach contour of baseline(a), CFJ-1(b) and CFJ-2(c)-Geometry-2, $\delta = 45°$, $\beta = 0°$, CFJ C_μ=0.08.

Table. 6 compares the CFJ-1 and 2 Geometry 2 with the baseline geometry. It indicates that the effectiveness of CFJ is not sensitive to the sweep angle and aspect ratio.

Table 6: C_L, P_c and $(C_L/C_D)_c$ of Geometry-2 and its CFJ designs, β=0°, δ=45°, CFJ C_μ=0.08.

Geometry	C_L	C_D	P_c	C_L/C_D	$(C_L/C_D)_c$	$\delta C_L/P_c$	ΔC_L	U_{inj}/U_∞	PR
Baseline	0.6894	0.2712	0	2.5424	2.5424	0	0%	-	-
CFJ-1	0.8282	0.3189	0.1702	2.1618	1.6933	0.8155	19.3%	1.063	1.035
CFJ-2	1.1822	0.4337	0.0594	2.7260	2.3976	8.2963	71.5%	3.028	1.038

Based on the results above, CFJ-2-Geometry-1 is the configuration with the optimal aerodynamic performance. Several parameter trade studies are then further conducted based on this optimal configuration.

3.2 Trade Study of Flap Deflection Angle

Fig. 13 shows the positions of the flap deflection angles studied for CFJ-2-Geometry-1, with δ=0°, 15°, 30°, 45° and 60° respectively. The flaps are rotated around the assumed hinge shown in Fig. 13.

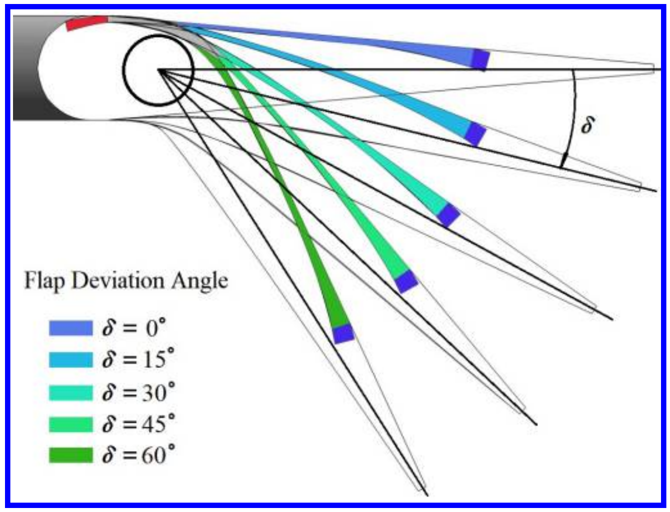

Figure 13: Different flap deflection angles for CFJ-2-Geometry-1, β=0°, θ=65°.

The coefficients of lift and drag, CFJ power, C_L/C_D and $(C_L/C_D)_c$ versus flap deflection angle δ are shown in Fig. 14(a). The lift difference is not large when δ is less than 30°. When δ is larger than 30°, the baseline lift coefficient becomes flat, whereas the CFJ-2's lift coefficient continues to grow linearly. At $\delta = 60°$, CFJ-2 increases the lift by 113.1% from 0.808 to 1.707, with the $(C_L/C_D)_c$ about the same as that of the baseline.

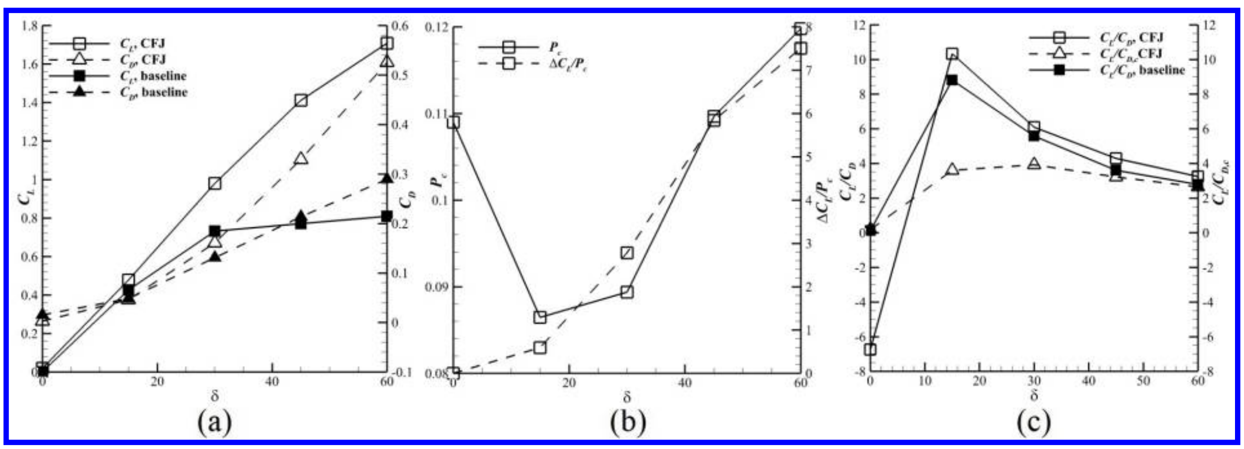

Figure 14: C_L, C_D, P_c, (C_L/C_D), $(C_L/C_D)_c$ and $\Delta C_L/P_c$ of CFJ-2-Geometry-1 with varying δ, compared with baseline, C_μ=0.08, β=0°.

The Mach contours comparing CFJ-2-Geometry-1 at $\delta = 60°$ (shown in Fig. 15(a), (b) and (c)) with the case at $\delta = 45°$ (Fig.15(d), (e) and (f))indicate that the flow is well attached at δ of 45° at C_μ of 0.08, but slightly separated on the flap for δ of 60°. A slightly larger C_μ should be able to fully attach the flow.

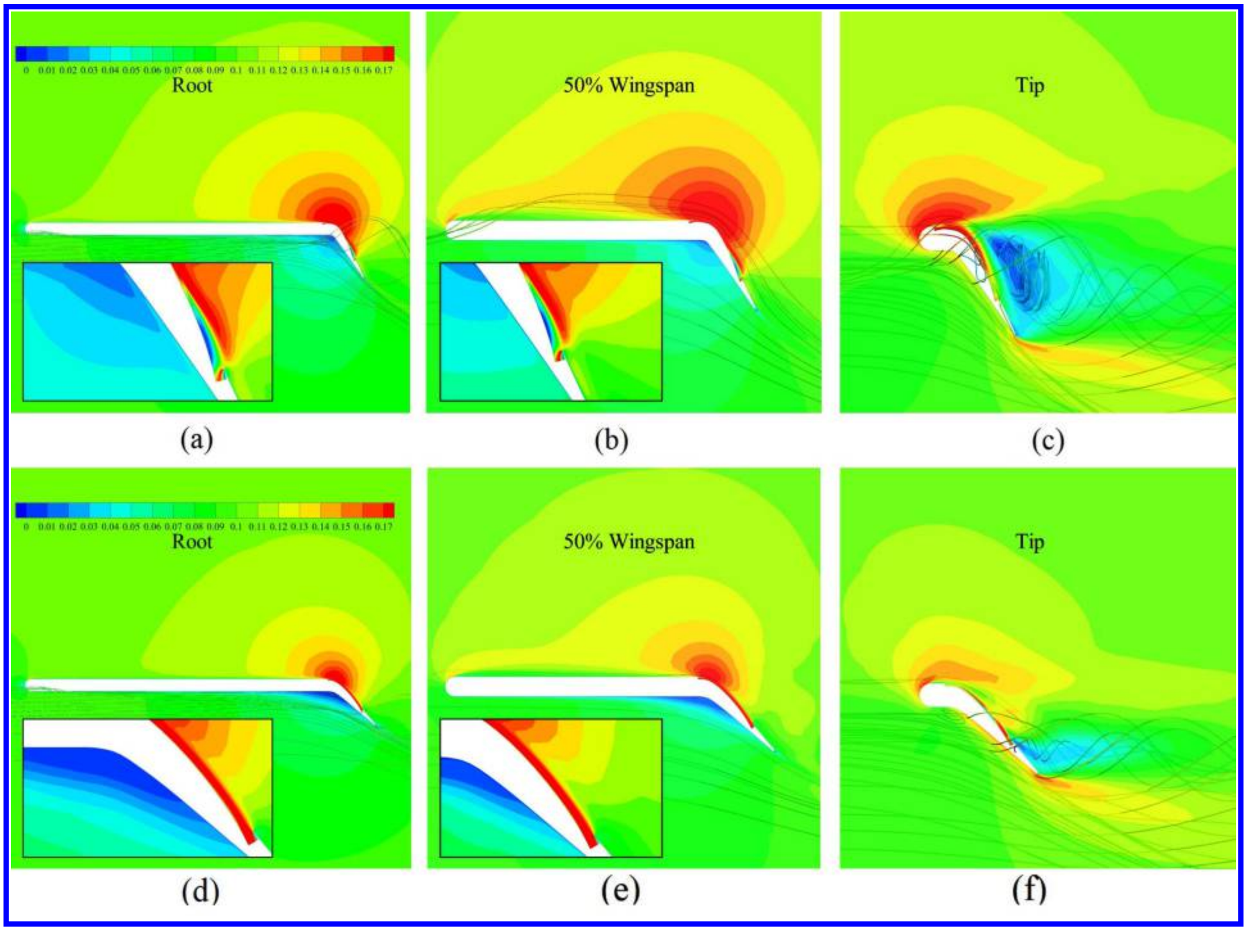

Figure 15: Flow pattern on the root, midspan and tip region of CFJ-2-Geometry-1 with flap lowered to $\delta = 60°$(a-c) and $\delta = 45°$(d-f), θ=65°.

3.3 Trade Study of CFJ Injection Location

In the CFJ-2 designs, the injection slot is placed along the flap deflection arc and can vary considerably. placed along the flap deflection arc and can vary considerably. An angular value θ is defined to describe the position of the injection duct outlet against the horizontal line on the left of the hinge location. Four injection duct outlet positions located from upstream to downstream (Inj_Loc 1, 2, 3, 4) are given in Fig. 16 with the θ angle of 65°, 100°, 140°, and 175°, respectively. The Inj_Loc 4 is located beyond the turning arc. All the four locations have the flow attached.

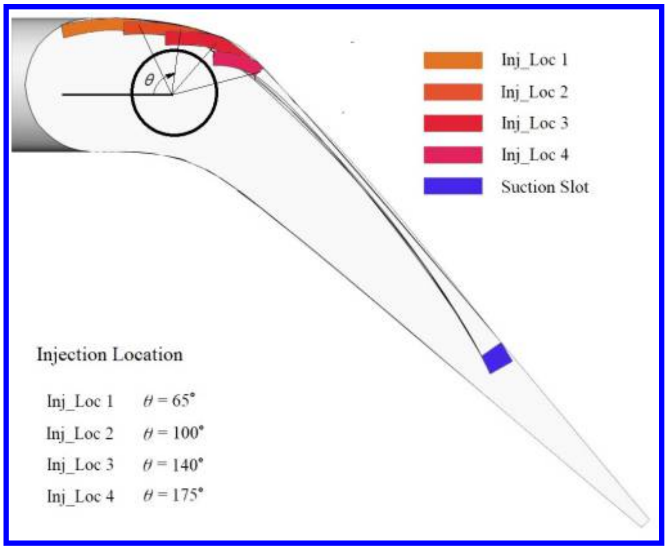

Figure 16: Sketch of the different CFJ injection location. δ=45°, θ=65°, 100°, 140° and 175°.

The coefficients of lift, drag, CFJ power, C_L/C_D, $(C_L/C_D)_c$ versus θ are plotted in Fig. 17(a). From upstream to downstream, the lift and drag are both reduced about 5%, but the CFJ power coefficient is reduced about 50%. This is because the main flow pressure is much lower than at the end of the turning due to the flow acceleration and it requires a low power to inject the flow.

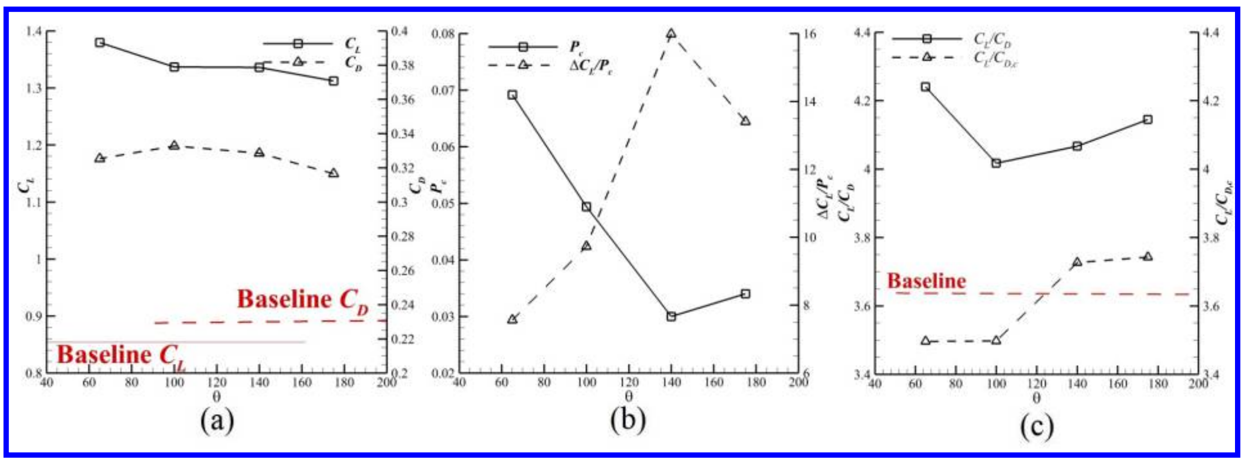

Figure 17: C_L, C_D, P_c, (C_L/C_D), $(C_L/C_D)_c$ and $\Delta C_L/P_c$ of CFJ-2-Geometry-1 with varied θ. C_μ=0.08, β=0°, δ=45°.

As the result, the $(C_L/C_D)_c$ increased by 6.69% to 3.7342 at $\theta = 175°$, 2.5% higher than that of the baseline (C_L/C_D).

3.4 Trade Study of C_μ

C_μ is varied to study its effect on the aerodynamic performance and power consumption for CFJ-2-Geometry-1, and the results are plotted in Fig. 18. The configuration has δ=45°, β=0°, CFJ $h_{inj} = 0.4\%MAC$, and $\theta = 65°$. Fig. 18 indicates:

a)C_μ needs to be greater than 0.01 to have enhancement effect. When it is less than that, the lift decreases.

b) At low C_mu range from 0.01 to 0.04, the lift coefficient rapidly increases with a steep slope (Fig. 18(a)) and the P_c increases at a slower pace. The highest lift-drag ratio occurs at C_μ=0.02, with $(C_L/C_D)_c$=4.077, slightly higher than $(C_L/C_D)_c$=4.034 at C_μ=0.03.

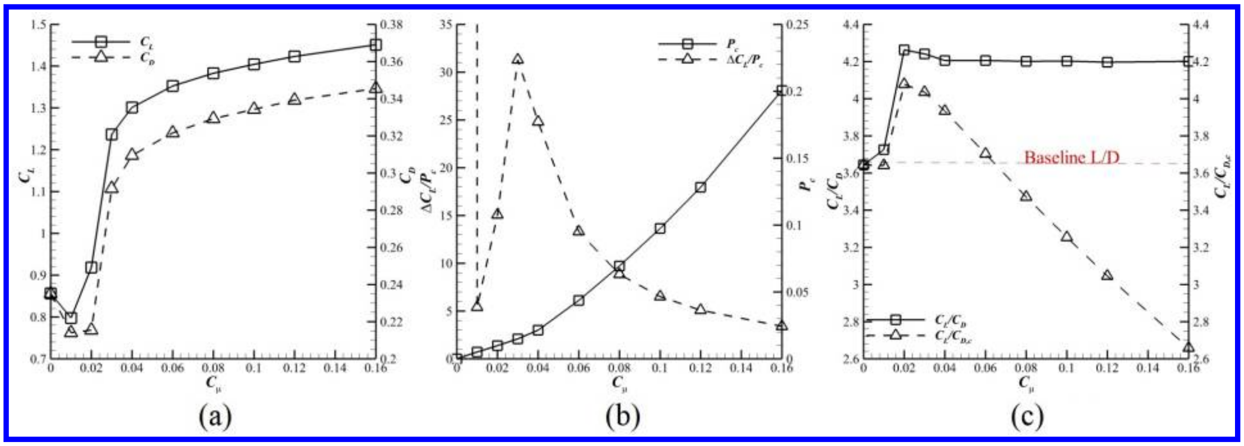

Figure 18: C_L, C_D, P_c, $\Delta C_L/P_c$ and $(C_L/C_D)_c$ of CFJ-2-Geometry-1 versus C_μ, δ=45°, β=0°, θ=65°.

Fig. 19 shows the Mach contour of CFJ-2-Geometry-1 with several small CFJ C_μs of 0.01(a), 0.03(b) and 0.06(c). It can be seen that, with C_μ=0.01, massive separation on the flap still exists and a large vortex is observed along the spanwise direction. When C_μ increases to 0.03, which leads to the surge of C_L in Fig. 18, the separation is almost removed and vortices are not observed any more except tip region.

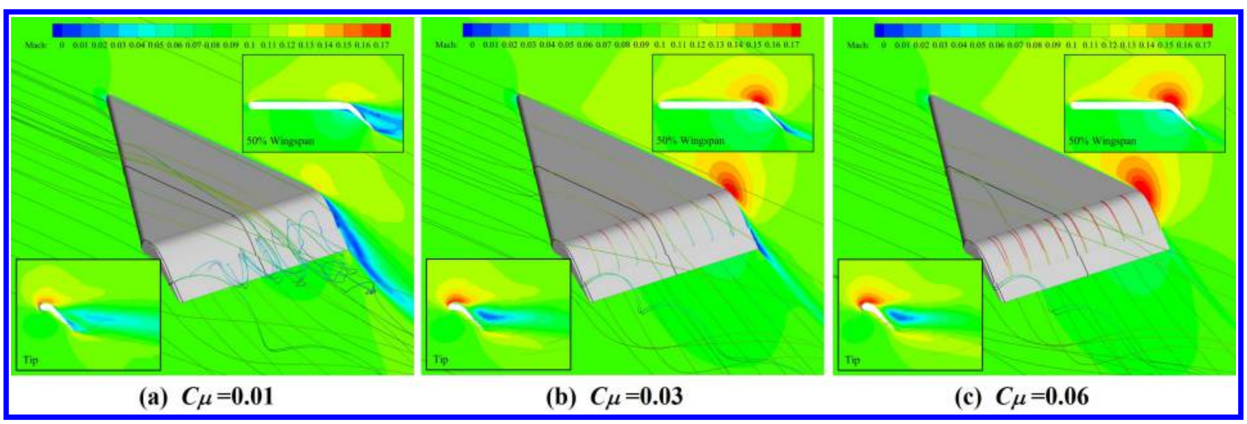

Figure 19: Mach contour of CFJ-2-Geometry-1, $\delta = 45°$, $\beta = 0°$, CFJ C_μ=0.01(a), 0.03(b) and 0.06(c).

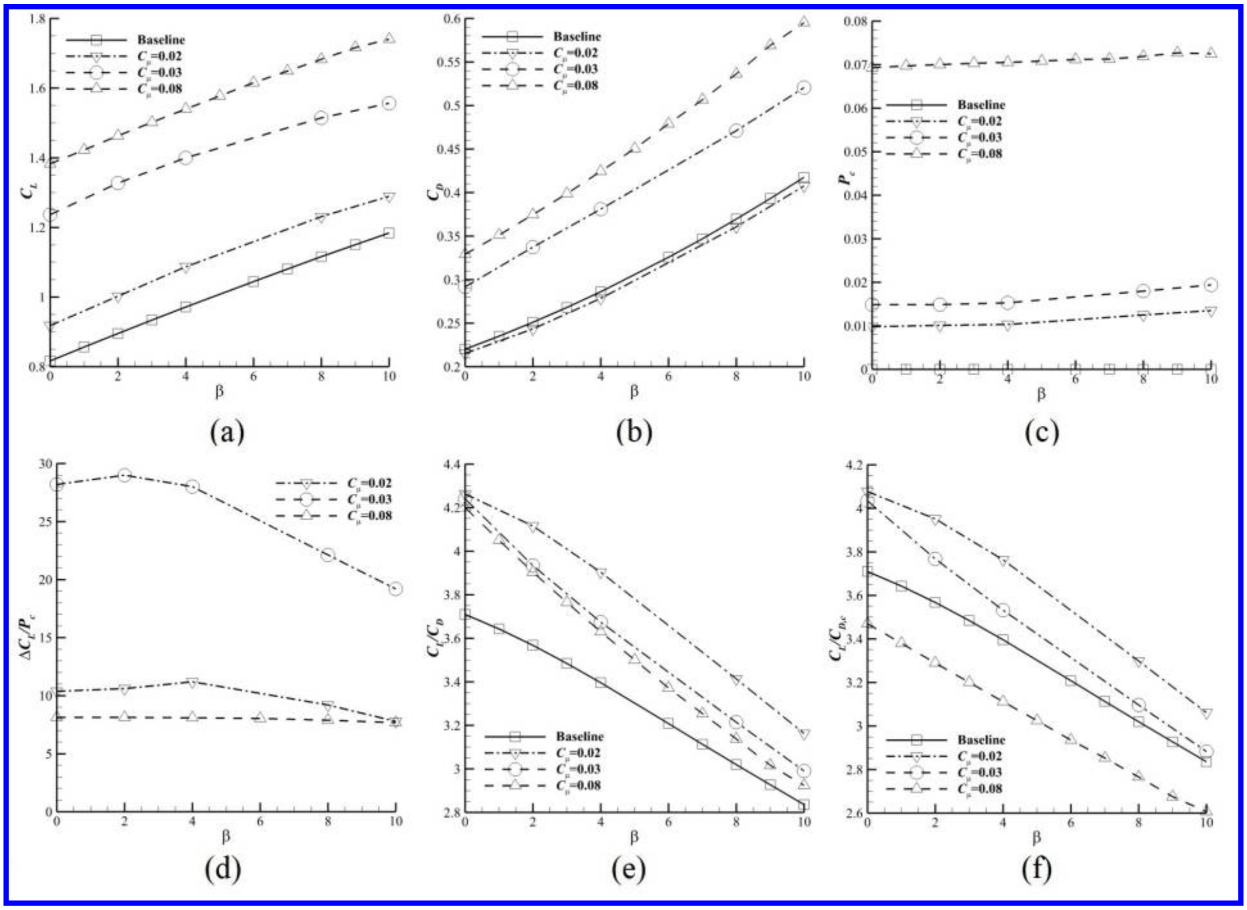

Figure 20: C_L, C_D, P_c, C_D/P_c and $(C_L/C_D)_c$ of CFJ-2-Geometry-1 versus varied βs, δ=45°, θ=65°.

Fig. 20 presents the coefficient of lift, drag, CFJ power, C_L/C_D and $(C_L/C_D)_c$ for different C_μ with variation of incidence angle from $\beta = 0°$ to 10°.

With the constant C_μ, the coefficient of lift and drag linearly increase with the incidence angle β, whereas the CFJ power coefficient is fairly constant. The C_L/C_D and $(C_L/C_D)_c$ linearly decreases with β. At low C_μ of 0.02, the $(C_L/C_D)_c$ is higher than that of the baseline with the C_L also higher. For this geometry with injection at $\theta = 65°$, the $(C_L/C_D)c$ is lower than that of the baseline while the lift coefficient is substantially greater. With the injection moved to θ=175°, the CFJ power coefficient is reduced by 50% as shown in Fig. 17. The $(C_L/C_D)c$ then surpasses the value of the baseline wing as also shown in Fig. 17 and Table 5.

4 Conclusions

Numerical study is carried out to investigate flapped delta wing low speed performance with coflow jet (CFJ) flow control at Mach number of 0.1. Two delta wings formed by thin supersonic airfoils with aspect ratio of 2 and 0.67 and sweep angle of 53° and 63.5° are studied, but only detailed results for the wing with aspect ratio of 2 are presented. The simulation is validated very well with the experiment. The flap has a constant chord along span and is 24% of the root chord. CFJ is applied in two ways: one on top of the main front part of the delta wing and the other is on the deflected flap. Both are effective, but the CFJ applied on the deflected flap is much more effective with flow attached up to the flap deflection angle of 60°. It has substantially higher lift coefficient enhancement and lower CFJ power consumption for the same C_μ.

With $C_\mu = 0.08$ and CFJ applied on the flap, the delta wing with AR of 2 improves C_L by 113.1% at a flap deflection angle of 60°, whereas $(C_L/C_D)_c$ is about the same as that of the baseline delta wing with no flow control at the same flap deflection angle.

Trade studies are conducted to investigate the effect of delta wing incidence angle (β), flap deflection angle (δ), CFJ injection slot location, CFJ momentum coefficient C_μ. The trade study of the incidence angle shows that the CFJ used on the flap is effective at least up to β of 20° with the appearance of the delta wing leading edge vortex. The flap deflection angle study indicates that the baseline delta wing's lift coefficient becomes flat when the flap deflection angle is greater than 30°, whereas the delta wing with CFJ flap has the lift coefficient increased linearly to the deflection angle of 60° studied. The trade study of the injection location shows that the lift and drag coefficient are decreased about 5% when the injection is moved from upstream of the flap deflection shoulder to downstream of the shoulder, but the CFJ power coefficient is reduced by 50%. The injection momentum coefficient trade study indicates that the lift coefficient is enhanced most rapidly at low C_μ value range from 0.01 to 0.04 with a steep slope, whereas the CFJ power coefficient P_c increases at a slower pace. At C_μ of 0.03, the CFJ flapped delta wing achieves C_L of 1.23, C_L/C_D of 4.21, and $(C_L/C_D)_c$ of 4.034. Compared with the baseline flapped delta wing with C_L of 0.856 and C_L/C_D of 3.64, the CFJ delta wing achieves an increase of lift coefficient by 44% and C_L/C_D by 15.6% respectively with the CFJ power coefficient of 0.013.

This study is only an initial effort to apply CFJ flow control to thin supersonic delta wing with a flap. It shows that CFJ is very effective to substantially increase lift coefficient at very low energy expenditure, which has great potential to enhance the supersonic aircraft's low-speed performance.

5 Acknowledgment

The simulations are conducted on Pegasus super-computing system at the Center for Computational Sciences (CCS) at the University of Miami.

Disclosure: The University of Miami and Dr. Gecheng Zha may receive royalties for future commercialization of the intellectual property used in this study. The University of Miami is also equity owner in CoFlow Jet, LLC, licensee of the intellectual property used in this study.

References

[1] H. Welge, C. Nelson, and J. Bonet, "Supersonic vehicle systems for the 2020 to 2035 timeframe," in *28th AIAA Applied Aerodynamics Conference*, p. 4930, 2010.

[2] R. E. Curry and L. R. Owens, "Ground-effect characteristics of the tu-144 supersonic transport airplane," 2003.

[3] R. A. Rivers, E. B. Jackson, C. G. Fullerton, T. H. Cox, and N. H. Princen, "A qualitative piloted evaluation of the tupolev tu-144 supersonic transport," 2000.

[4] E. Gordon, "Technical specs, http://www.concordesst.com/concordeb.html," 2001.

[5] D. A. Garvin, "Boeing 767: From concept to production (a)," 1988.

[6] D. Mavris and M. Kirby, "Takeoff / landing assessment of an hsct with pneumatic lift augmentation," in *37th Aerospace Sciences Meeting and Exhibit*, p. 534, 1998.

[7] R. L. L. Englar, "Circulation control for high lift and drag generation on stol aircraft," *Journal of Aircraft*, vol. 12, no. 5, pp. 457–463, 1975.

[8] G.-C. Zha and D. C. Paxton, "A Novel Flow Control Method for Airfoil Performance Enhancement Using Co-Flow Jet." *Applications of Circulation Control Technologies*, Chapter 10, p. 293-314, Vol. 214, Progress in Astronautics and Aeronautics, AIAA Book Series, Editors: Joslin, R. D. and Jones, G.S., 2006.

[9] G.-C. Zha, W. Gao, and C. Paxton, "Jet Effects on Co-Flow Jet Airfoil Performance," *AIAA Journal, No. 6,*, vol. 45, pp. 1222–1231, 2007.

[10] G.-C. Zha, C. Paxton, A. Conley, A. Wells, and B. Carroll, "Effect of Injection Slot Size on High Performance Co-Flow Jet Airfoil," *AIAA Journal of Aircraft*, vol. 43, 2006.

[11] G.-C. Zha, B. Carroll, C. Paxton, A. Conley, and A. Wells, "High Performance Airfoil with Co-Flow Jet Flow Control," *AIAA Journal*, vol. 45, 2007.

[12] Wang, B.-Y. and Haddoukessouni, B. and Levy, J. and Zha, G.-C., "Numerical Investigations of Injection Slot Size Effect on the Performance of Co-Flow Jet Airfoil," *Journal of Aircraft*, vol. Vol. 45, No. 6,, pp. pp.2084–2091, 2008.

[13] B. P. E. Dano, D. Kirk, and G.-C. Zha, "Experimental Investigation of Jet Mixing Mechanism of Co- Flow Jet Airfoil." AIAA-2010-4421, 5th AIAA Flow Control Conference, Chicago, IL, 28 Jun - 1 Jul 2010.

[14] B. P. E. Dano, G.-C. Zha, and M. Castillo, "Experimental Study of Co-Flow Jet Airfoil Performance Enhancement Using Micro Discreet Jets." AIAA Paper 2011-0941, 49th AIAA Aerospace Sciences Meeting, Orlando, FL, 4-7 January 2011.

[15] A. Lefebvre, B. Dano, W. Bartow, M. Fronzo, and G. Zha, "Performance and energy expenditure of coflow jet airfoil with variation of mach number," *Journal of Aircraft*, vol. 53, no. 6, pp. 1757–1767, 2016.

[16] A. Lefebvre, G-C. Zha, "Numerical Simulation of Pitching Airfoil Performance Enhancement Using Co-Flow Jet Flow Control," *AIAA paper 2013-2517*, June 2013.

[17] A. Lefebvre, G-C. Zha, "Cow-Flow Jet Airfoil Trade Study Part I : Energy Consumption and Aerodynamic Performance," *32nd AIAA Applied Aerodynamics Conference, AIAA AVIATION Forum, AIAA 2014-2682*, June 2014.

[18] A. Lefebvre, G-C. Zha, "Cow-Flow Jet Airfoil Trade Study Part II : Moment and Drag," *32nd AIAA Applied Aerodynamics Conference, AIAA AVIATION Forum, AIAA 2014-2683*, June 2014.

[19] Lefebvre, A. and Zha, G.-C., "Trade Study of 3D Co-Flow Jet Wing for Cruise Performance." AIAA Paper 2016-0570, AIAA SCITECH2016, AIAA Aerospace Science Meeting, San Diego, CA, 4-8 January 2016.

[20] Lefebvre, A. and Dano, B. and Bartow, W. and Di Franzo, M. and Zha, G.-C., "Performance Enhancement and Energy Expenditure of Co-Flow Jet Airfoil with Variation of Mach Number." AIAA Paper 2013-0490, AIAA Journal of Aircraft, DOI: 10.2514/1.C033113, 2016.

[21] Yunchao Yang and Gecheng Zha, "Super-Lift Coefficient of Active Flow Control Airfoil: What is the Limit?." AIAA Paper 2017-1693, AIAA SCITECH2017, 55th AIAA Aerospace Science Meeting, Grapevine, January 9-13 2017.

[22] Y. Wang and G.-C. Zha, "Study of 3D Co-flow Jet Wing Induced Drag and Power Consumption at Cruise Conditions." AIAA Paper 2019-0034, AIAA SciTech 2019, San Diego, CA, January 7-11, 2019.

[23] Y. Wang, Y.-C. Yang, and G.-C. Zha, "Study of Super-Lift Coefficient of Co-Flow Jet Airfoil and Its Power Consumption." AIAA Paper 2019-3652, AIAA Aviation 2019, AIAA Applied Aerodynamics Conference, Dallas, Texas, 17-21 June 2019.

[24] Y. Wang and G.-C. Zha, "Study of Mach Number Effect for 2D Co-Flow Jet Airfoil at Cruise Conditions." AIAA Paper 2019-3169, AIAA Aviation 2019, AIAA Applied Aerodynamics Conference, Dallas, Texas, 17-21 June 2019.

[25] K.-W. Xu, Y. Ren, and G.-C. Zha, "Flow separation control by coflow wall jet." AIAA Paper 2021-2946, AIAA Aviation 2021, Virtual Events, Submitted to AIAA Journal, 2-6 Aug. 2021.

[26] Zha, G.C., Shen, Y.Q. and Wang, B.Y., "An improved low diffusion E-CUSP upwind scheme ," *Journal of Computer and Fluids*, vol. 48, pp. 214–220, Sep. 2011.

[27] G.-C. Zha and E. Bilgen, "Numerical Solutions of Euler Equations by Using a New Flux Vector Splitting Scheme ," *International Journal for Numerical Methods in Fluids*, vol. 17, pp. 115–144, 1993.

[28] G.-C. Zha and E. Bilgen, "Numerical Study of Three-Dimensional Transonic Flows Using Unfactored Upwind-Relaxation Sweeping Algorithm," *Journal of Computational Physics*, vol. 125, pp. 425–433, 1996.

[29] B.-Y. Wang and G.-C. Zha, "A General Sub-Domain Boundary Mapping Procedure For Structured Grid CFD Parallel Computation," *AIAA Journal of Aerospace Computing, Information, and Communication*, vol. 5, No.11, pp. 2084–2091, 2008.

[30] Y.-Q. Shen, G.-C. Zha, and B.-Y. Wang, "Improvement of Stability and Accuracy of Implicit WENO Scheme ," *AIAA Journal*, vol. 47, pp. 331–344, 2009.

[31] M. O. McKinney Jr and H. M. Drake, "Flight characteristics at low speed of delta-wing models," 1948.

[32] Z. Liu and G. Zha, "Transonic airfoil performance enhancement using co-flow jet active flow control," in *8th AIAA Flow Control Conference*, p. 3472, 2016.